

## Prediction of acoustic noise and vibration of a 24/16 traction switched reluctance machine

Liang, Jianbin; Jiang, James W.; Callegaro, Alan Dorneles; Bilgin, Berker; Dong, Jianning; Reeves, Debbie; Emadi, Ali

**DOI**

[10.1049/iet-est.2018.5031](https://doi.org/10.1049/iet-est.2018.5031)

**Publication date**

2020

**Document Version**

Final published version

**Published in**

IET Electrical Systems in Transportation

**Citation (APA)**

Liang, J., Jiang, J. W., Callegaro, A. D., Bilgin, B., Dong, J., Reeves, D., & Emadi, A. (2020). Prediction of acoustic noise and vibration of a 24/16 traction switched reluctance machine. *IET Electrical Systems in Transportation*, 10(1), 35-43. <https://doi.org/10.1049/iet-est.2018.5031>

**Important note**

To cite this publication, please use the final published version (if applicable).  
Please check the document version above.

**Copyright**

Other than for strictly personal use, it is not permitted to download, forward or distribute the text or part of it, without the consent of the author(s) and/or copyright holder(s), unless the work is under an open content license such as Creative Commons.

**Takedown policy**

Please contact us and provide details if you believe this document breaches copyrights.  
We will remove access to the work immediately and investigate your claim.

***Green Open Access added to TU Delft Institutional Repository***

***'You share, we take care!' - Taverne project***

**<https://www.openaccess.nl/en/you-share-we-take-care>**

Otherwise as indicated in the copyright section: the publisher is the copyright holder of this work and the author uses the Dutch legislation to make this work public.

# Prediction of acoustic noise and vibration of a 24/16 traction switched reluctance machine

ISSN 2042-9738

Received on 22nd May 2018

Revised 14th November 2018

Accepted on 18th June 2019

E-First on 20th August 2019

doi: 10.1049/iet-est.2018.5031

www.ietdl.org

Jianbin Liang<sup>1</sup> ✉, James W. Jiang<sup>1</sup>, Alan Dorneles Callegaro<sup>1</sup>, Berker Bilgin<sup>1</sup>, Jianning Dong<sup>2</sup>, Debbie Reeves<sup>3</sup>, Ali Emadi<sup>1</sup>

<sup>1</sup>McMaster Automotive Resource Centre (MARC), McMaster University, Hamilton, Canada

<sup>2</sup>Delft University of Technology, Delft, The Netherlands

<sup>3</sup>MSC Software, Michigan, USA

✉ E-mail: liangj31@mcmaster.ca

**Abstract:** This study presents a numerical modelling approach for the prediction of vibration and acoustic noise for a 24/16 traction switched reluctance machine (SRM). The numerical modelling includes the simulation of electromagnetic force in JMAG, the calculation of natural frequencies and the simulation of vibration and acoustic noise in ACTRAN. Considerations in the modelling of geometries, meshing and contacts of the 24/16 SRM are discussed to ensure the accuracy of the numerical simulation. Two-dimensional fast Fourier transform (FFT) is applied to the radial nodal force at the stator pole tip to analyse the dominant harmonics. FFT is also applied to the simulated surface displacement of the housing and the sound pressure at 2000 rpm to analyse their dominant frequency components. The dominant harmonics for the vibration and acoustic noise at 2000 rpm are confirmed. The numerical modelling method presented in this study can also be applied to the other SRMs and electric machines to predict the vibration behaviour and the radiated acoustic noise.

## 1 Introduction

Switched reluctance machines (SRMs) are attracting attention from academia and industry. SRMs have also been considered as a potential candidate for industrial applications in recent years because of their simple structure, robust design, high-temperature tolerance and lack of rare earth material [1–3]. However, compared to induction machines and permanent magnet synchronous machines, acoustic noise radiated from SRM can be more severe [4]. This demerit has been a challenge for the applications of SRMs in electric vehicles and hybrid electric vehicles (HEVs).

Much effort and attempt have been made to model the vibration behaviour and acoustic noise of SRMs. In the literature, two kinds of approaches in the prediction of acoustic noise for electric machines are reported: the statistical and deterministic methods. Although the statistical approach, which is based on statistical energy analysis, is applicable to complex structures in the high-frequency range, this method cannot provide results with high accuracy at the low-frequency range [5]. The deterministic approach includes analytical and numerical methods. The analytical method can provide a fast and computationally efficient way for the acoustic noise prediction in both low and high frequencies [6–11]. Therefore, it is preferred in the design, optimisation and control of electric machines. On the other hand, the numerical model is more precise because more structural details can be considered in the modelling. Even though the numerical method is more time-consuming and computationally inefficient in the high-frequency range [5], it is useful to verify the acoustic results from the analytical method. For the numerical method, the prediction of the vibration and the acoustic noise of an electric machine is often based on three numerical models: an electromagnetic finite element analysis (FEA) model for the simulation of electromagnetic forces, a structural model for the simulation of vibration and an acoustic numerical model for the coupling between the aforementioned models and the acoustic simulation. The accuracy of the predicted vibration and acoustic noise depends on both the accuracy of the acoustic model and the input data. The input data includes the simulation of electromagnetic force and the calculation of natural frequencies of SRMs [5]. A few studies in the literature present the details of a

precise vibration and acoustic noise model, e.g. modelling and meshing of the structure. However, most of the numerical acoustic models in the literature are based on simplified geometries or models. The effect of winding and housing has not been considered in [12]. A precise modelling of vibrating structure and the meshing of the structure were not reported in [12–15].

In this paper, a detailed numerical modelling approach to predict the vibration and acoustic noise of a 24/16 SRM is presented. The modelling process is illustrated in the flow chart in Fig. 1. It couples electromagnetic analysis in JMAG, and modal, vibration and acoustic analysis in ACTRAN. Compared to previous practice in the literature mentioned above, the modelling approach in this paper is able to take into account the effects of winding and housing. Detailed considerations and procedures to ensure the accuracy of the results and reduce the computational cost are presented in Section 3. This paper also discusses a useful method to quantitatively obtain and analyse the relationships between dominant harmonics of the electromagnetic force, dominant vibration mode, vibration (or surface displacement) and the radiated acoustic noise.

## 2 Design of a 24/16 SRM for hybrid electric vehicle powertrains

The vibration and acoustic analysis in this paper is performed on a 24/16 SRM designed for traction application in HEVs. Compared to combustion engines, which have a more broadband noise in the lower frequency range, SRMs in traction application might radiate noise at mid-frequency range or high-frequency range. Therefore, acoustic analysis of SRMs for traction applications is necessary [13].

The 24/16 SRM in this paper is designed to achieve the same torque-speed envelop of the interior permanent magnet synchronous motor (IPMSM) used in the 2010 Prius powertrain [1]. Table 1 compares the motor specifications of the designed 24/16 SRM and the IPMSM used in the 2010 Prius powertrain. The stator outer diameter and total axial length of the active material in the 24/16 SRM are exactly the same as IPMSM used in the 2010 Prius powertrain. Both motors can achieve similar peak power [1].

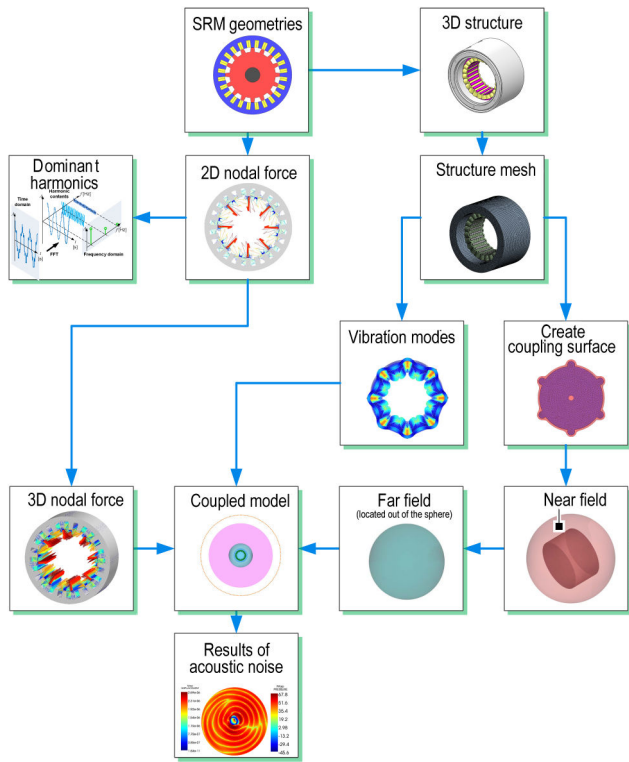


Fig. 1 Procedures for acoustic modelling of the 24/16 SRM

Table 1 Comparisons of the Prius 2010 traction motor and the 24/16 SRM [1]

Parameter	2010 Prius	24/16 SRM
stator outer diameter (mm)	264	264
total axial length of active material (mm)	108	108
air gap length (mm)	0.73	0.5
lamination thickness (mm)	0.305	0.1
slot fill factor	0.54	0.54
DC side voltage (V)	650	650
maximum peak current (A)	240	240
RMS current constraint (A)	140	140
motor peak power rating (kW)	60	60
rotational speed rating (rpm)	13,500	13,500

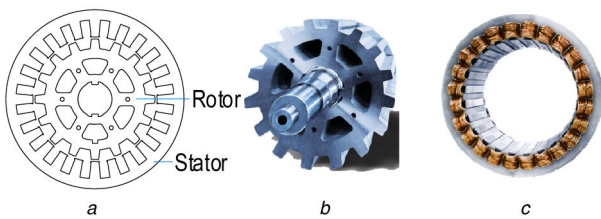


Fig. 2 Geometries of the rotor and stator in the 24/16 SRM (a) CAD geometry, (b) Stator core, (c) Rotor core

The 24/16 SRM can also achieve similar peak efficiency as that of the IPMSM used in the 2010 Prius powertrain. The peak efficiency of the 24/16 SRM is 96.5% at 7500 rpm and 60 Nm. Fig. 2 shows the geometries of the rotor and stator in the 24/16 SRM. The laminations are provided by Cogent Power Inc. Its grade and thickness are NO10 and 0.1 mm, respectively.

### 3 Numerical acoustic modelling of 24/16 SRM

#### 3.1 Numerical modelling procedure

The procedures for the numerical modelling of vibration and the acoustic noise are shown in Fig. 1. The acoustic simulation needs the nodal force and the simulated vibration modes as inputs.

Starting with the SRM geometries, the 2D nodal force can be generated by electromagnetic simulation in JMAG. The nodal force is a function of both time and stator circumferential positions. Two-dimensional fast Fourier transform (FFT) is applied to the nodal forces to analyse the dominant harmonics. Then, the 2D nodal force is extruded to the 3D nodal force which is one of the inputs to the coupled noise and vibration model.

As shown in Fig. 1, starting with the 3D motor structure, the structural meshing can be performed in ANSYS Workbench. The meshed structure is used in the simulation of vibration modes and the acoustic modelling in ACTRAN. The natural frequencies and their corresponding mode shapes will be simulated in ACTRAN. The acoustic modelling is also performed in ACTRAN, including the creation and meshing of coupling surfaces, near field and far field. The coupling surfaces, including the structural coupling surface and the acoustic coupling surface, are the boundary conditions for the simulation of vibration and acoustic noise, respectively. Taking the 3D nodal force and the simulated mode shape as inputs, the coupled vibration and noise can be simulated, and the acoustic noise results are obtained.

The construction of the acoustic modelling is shown in Fig. 3a. The near field is the field in which the nature of the sound wave depends on the vibration of the structure. The far field is the field in which the nature of the sound wave depends on the propagation medium, air. The near field will be modelled with finite elements while the far field is modelled with infinite elements. Infinite elements are different from the finite elements. Infinite element has an exponential term in its shape function, which is better to describe the unbounded property of the far field [16]. The infinite element method is used to simulate the acoustic behaviour in the far field. It is beneficial to adopt finite elements and infinite elements in the meshing for different fields. It helps to model the non-reflecting boundary conditions of the far field and provides a direct numerical estimate of the solution at all points in the far field. It has also been proven to be efficient in solving acoustic scattering problems [16, 17]. The element size of the structural meshing and the acoustic meshing as well as the connections between parts will be discussed later. The near field is modelled by a sphere (see Fig. 3a) in the acoustic modelling. In order to ensure the accuracy of the simulation at the expense of a low computation cost, the sphere for the near field should be at least one wavelength thick, which is measured from the surface of the SRM housing.

Sound pressure or sound power can be used to describe the acoustic noise level radiated from the vibrating structure. In this paper, virtual microphones are used to measure the sound pressure of the acoustic noise radiated from the 24/16 SRM. As shown in Fig. 3b, the virtual microphones are located in circles. The captured sound pressure from three virtual microphones is shown in Fig. 3c. These three virtual microphones are located at 0°, 45° and 90°, respectively. Since there are differences in the amplitudes of the sound pressure captured by the three microphones, their positions should be selected wisely to show the characteristics of the acoustic noise in the 24/16 SRM. Virtual microphones are located in three arcs in the sphere surface, as shown in Fig. 4a. The three arcs are in three planes. Each plane has a spatial angle of 60° from each other. The placement of the virtual microphones in this paper is based on ISO 3744 standard. As shown in Fig. 5, a total of 20 virtual microphones are placed in a hemisphere with a radius of 1 m. Figs. 5a and b are the front view and top view of the hemisphere, respectively.

Virtual displacement sensors can also be mounted on the surface of the housing. This is beneficial for analysing the correlation between the vibration of the structure and the radiated noise. Basically, the virtual displacement sensors should be mounted on the housing surface where maximum displacement appears. The virtual displacement sensors in this paper are placed in the same axial position (see Fig. 4b). The circumferential positions of the virtual displacement sensors are on the back iron aligned with the stator pole because most of the force is applied on the stator poles. The larger magnitude of vibration will be captured in this way.

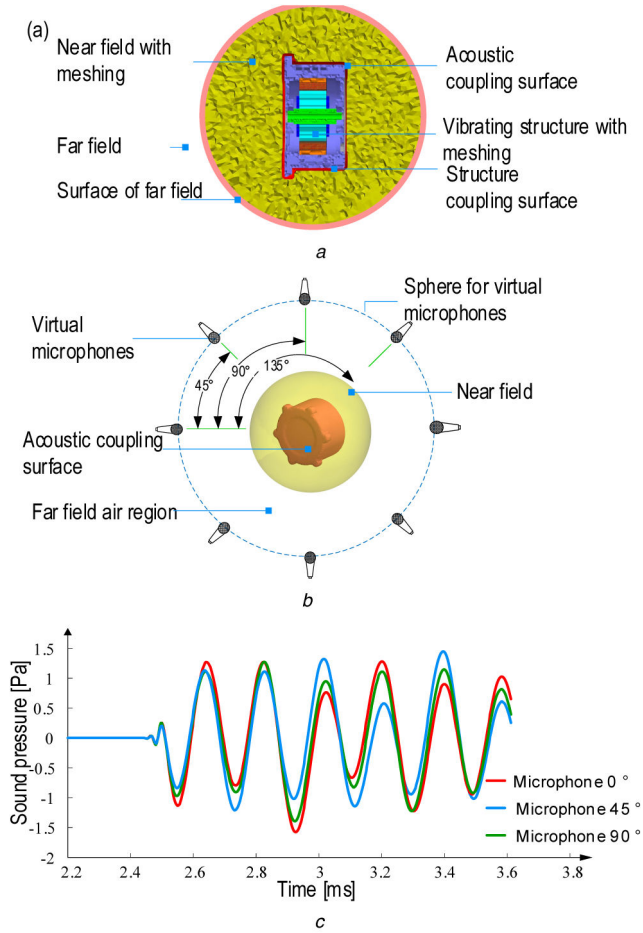


**Fig. 3** Acoustic numerical modelling  
(a) Acoustic model, (b) Positions of virtual microphones, (c) Sound pressure captured by three virtual microphones at different positions, motor speed 12,000 rpm

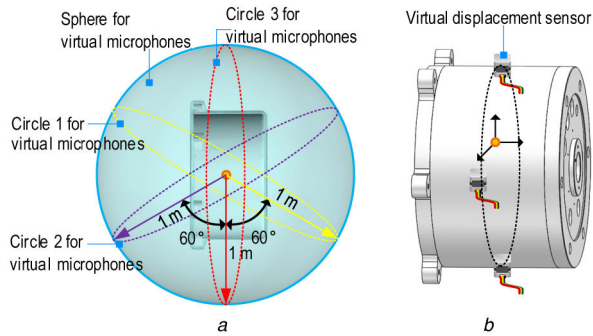


**Fig. 4** Positions of the virtual sensors  
(a) Virtual microphones, (b) Virtual displacement sensor

### 3.2 Calculation of nodal force in the 24/16 SRM

In order to obtain the nodal forces in the air gap, 2D electromagnetic FEA is first performed in JMAG. Fig. 6a shows the force vectors on the SRM at a certain time step when the motor is operating at 2000 rpm. Then the 2D nodal force is extended in the axial direction to generate the 3D nodal force, as shown in Fig. 6b. The nodal forces can be divided into two parts based on their directions: radial nodal forces and tangential nodal forces. In this paper, the radial and tangential nodal forces are both considered in the coupled simulation of vibration and acoustic noise.

The radial nodal force at the stator pole tip is extracted as shown in Fig. 7. For a certain time step (e.g. at  $t = 0.6$  s), there are eight major peaks in the circumferential position, because in a three-phase 24/16 SRM there are eight stator poles per phase. For a certain spatial position (e.g. at the stator spatial position of 110 mech. deg.), there is only one major pulsation on the radial force

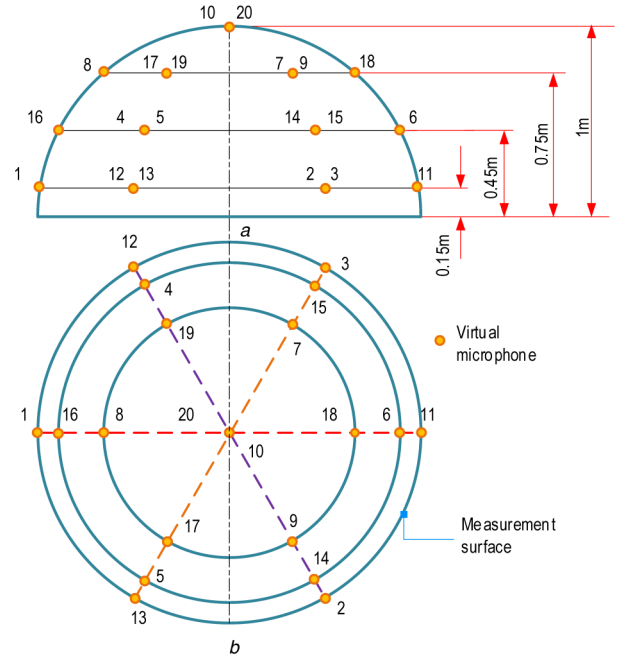


**Fig. 5** Positions of the virtual microphones for a hemispherical measurement surface based on ISO 3744 standard  
(a) Front view of the hemisphere, (b) Top view of the hemisphere

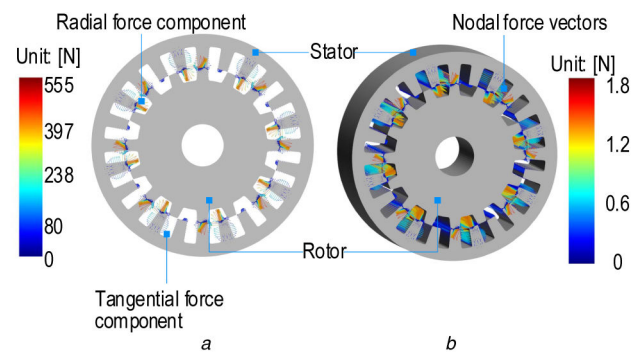


**Fig. 6** Nodal force at 2000 rpm  
(a) 2D nodal force, (b) 3D nodal force

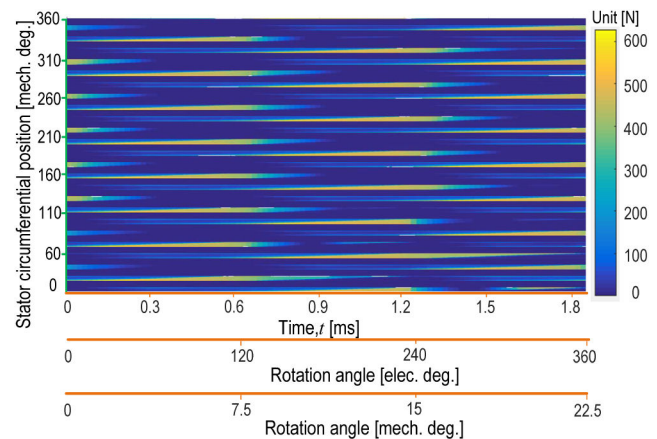


**Fig. 7** Radial nodal force at the stator pole tip of the 24/16 SRM at 2000 rpm

waveform with time because in every electrical cycle each phase is excited once. Then, 2D FFT is applied on the radial nodal force in the time domain and stator spatial domain to analyse the dominant harmonics of the radial nodal forces. This is important and necessary in order to understand the dominant harmonics which lead to the highest magnitude of vibration and noise. The results and the discussion of the harmonics of the radial force will be presented in Section IV.

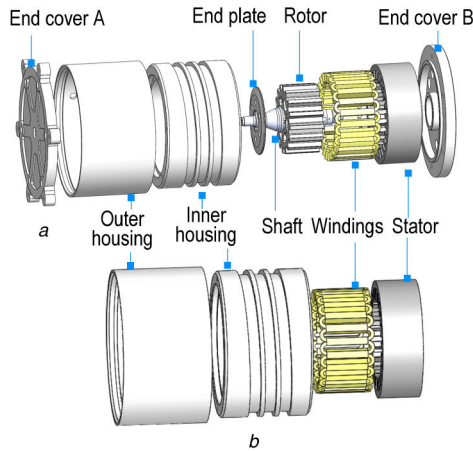


**Fig. 8** 3D geometry of the 24/16 SRM for numerical acoustic modelling  
(a) The complete structure, (b) Housing-stator-windings structure

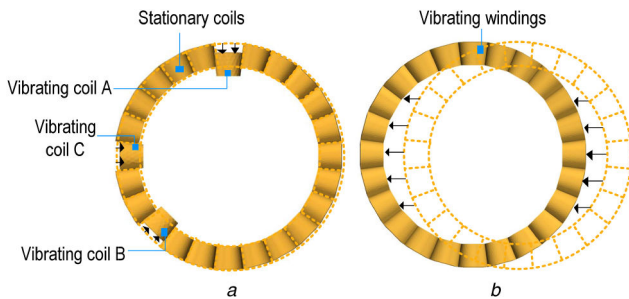


**Fig. 9** Vibration mode of windings and a single coil  
(a) A single coil, (b) The whole windings

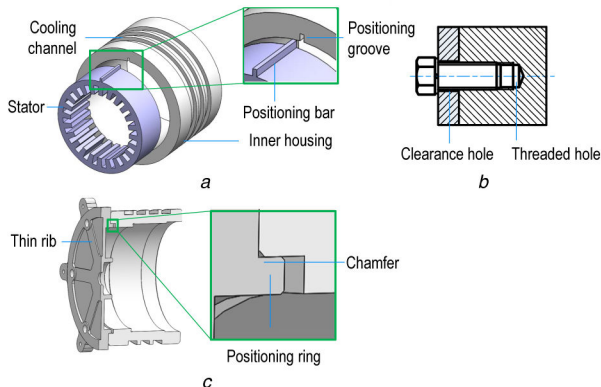


**Fig. 10** Small features for structural simplification  
(a) Positioning bar and groove, (b) Clearance hole and threaded hole, (c) Thin rib, positioning ring and chamfer

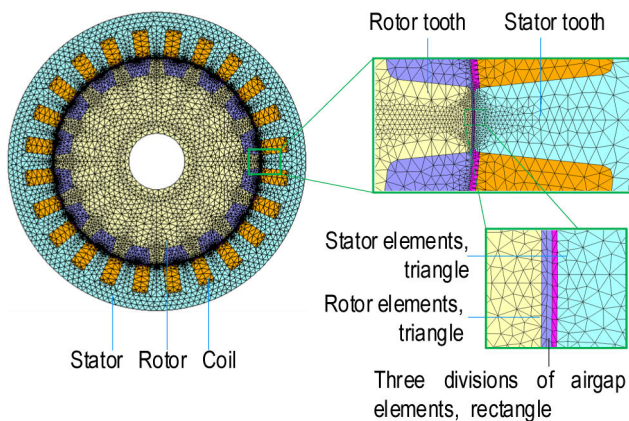


**Fig. 11** Meshing for the simulation to generate the nodal force model

### 3.3 Considerations in the modelling of geometry

The full assembly of the 24/16 SRM is shown in Fig. 8a. It includes the end plates, end covers, shaft, stator, housing and the rotor. For interior-rotor SRMs, literature reports that the vibration of the stator and the housing is the main source of acoustic noise [14, 15]. Therefore, the acoustic model presented in this paper only includes the housing, stator and the windings (see Fig. 8b).

The accuracy of the predicted acoustic noise is greatly affected by the accuracy of the model. The 3D geometry of the vibrating SRM should be built up so that it is close to the actual prototyped SRM, and the natural frequency can be calculated accurately. The concentrated windings have lumped mass effect, stiffness and damping effect on the stator poles. The geometry of the coil should be modelled accurately to get the correct volume and mass of the coils, which will affect the calculation of the natural frequencies of the vibrating structure. If a coil has no connection with other coils, it will vibrate separately, as shown in Fig. 9a. This will generate many extra and unrealistic vibration modes of a single coil, which will increase the computation cost of the acoustic simulation. However, the coils of the same phase are connected together. All the coils are assumed to be integrated and thus the windings will vibrate as a whole as shown in Fig. 9b.

In the numerical method, equations are solved at different nodes and elements in the meshed structure and thus it is necessary to reduce the number of nodes and elements to decrease the complexity of the computation. The geometry of the stator should be without structural simplification. However, the small features of housing can be simplified to reduce the computation cost. As shown in Fig. 10, there are many small features on the housing, e.g. clearance holes, screw holes, positioning grooves and ring, thin rib and chamfers. It takes finer meshing on these small features, which will increase the number of nodes and elements in the meshed structure. All these small features can be removed. The coolant channel is kept since it has great effect on the stiffness and the mass of the housing. It should be noted that the overall geometry of the SRM should be preserved, and the mass should be very close to the real structure, which is one of the keys to making good mesh for both structure and acoustic model.

### 3.4 Meshing in the numerical modelling

Proper and efficient meshing is important for numerical simulation. Considering the computation cost, the element size should not be too small. Few literatures report the calculation of element size in numerical modelling for the noise, vibration and harshness (NVH) prediction. In this section, the meshing will be discussed in detail.

Three kinds of meshing are necessary in the presented numerical model for the NVH simulation. The first one is the meshing for the electromagnetic model in JMAG to simulate the nodal force. The second kind is the structural meshing performed in ANSYS Workbench. The meshed structure will be used to calculate the natural frequencies and the simulation of the vibration. The third kind is the acoustic meshing in ACTRAN. The acoustic meshing will be generated in the near field, far field and the coupling surfaces.

Fig. 11 shows the 2D simulation of the nodal force in JMAG. The nodal force changes with time and spatial position. The meshing in the electromagnetic analysis is generated in JMAG. Fine meshing is generated in the air gap, rotor pole tips and stator pole tips, while a coarse mesh is generated in the regions that are away from the air gap.

The mesh quality is important for the accuracy of the electromagnetic FEA simulation. The air gap has the finest meshing and rectangle elements are used. For rectangle elements in the air gap, the circumferential length and the radial length of the rectangle elements should be determined.

The radial length of the rectangle element,  $E_{\text{Airgap, Radial}}$ , can be determined by

$$E_{\text{Airgap, Radial}} = \frac{L_{\text{Airgap, Radial}}}{N_{\text{RadDivisions}}} \quad (1)$$

where  $L_{\text{Airgap, Radial}}$  is the radial length of the airgap and  $N_{\text{RadDivisions}}$  is the number of radial divisions. As shown in Fig. 11, the number of radial divisions is 3. The radial length of the airgap,  $L_{\text{Airgap, Radial}}$ , is the airgap length, which has been determined by the designers in the design stage of the SRM.

The circumferential length of the airgap can be calculated as follows:

$$E_{\text{Airgap, Circ}} = E_{\text{Airgap, Radial}} \times \alpha \quad (2)$$

where  $\alpha$  is the aspect ratio.  $\alpha$  should be defined by the designers based on the required meshing quality and the computation cost. Theoretically, the ideal aspect ratio is one, which makes it a square element. However, considering the computation cost, the actual aspect ratio should not be too small. If the aspect ratio is 1, the circumferential length of the element in the air gap will be the same as its radial length. Therefore, a proper value of aspect ratio should be determined based on the meshing quality and computation cost. The range of aspect ratio should be between 1 and 10.

The number of circumferential divisions,  $N_{\text{CircDivisions}}$ , can be determined by

$$N_{\text{CircDivisions}} = \frac{L_{\text{Airgap, Circ}}}{E_{\text{Airgap, Circ}}} \quad (3)$$

where  $L_{\text{Airgap, Circ}}$  is the circumference length of the airgap.

The circumferential length of the airgap,  $L_{\text{Airgap, Circ}}$ , can be calculated by

$$L_{\text{Airgap, Circ}} = 2\pi R_{\text{Airgap, Radius}} \quad (4)$$

where  $R_{\text{Airgap, Radius}}$  is the radius of the airgap.

The element size of the rotor tip should also have fine meshing, which can be calculated by

$$E_{\text{Edge, Rotor}} = \frac{2\pi R_{\text{Rotor}}}{N_{\text{CircDivisions}}} \quad (5)$$

where  $R_{\text{rotor}}$  is the radius of the rotor outer radius.

The element size of the stator tip can be calculated by

$$E_{\text{Edge, Stator}} = \frac{2\pi R_{\text{Stator}}}{N_{\text{CircDivisions}}} \quad (6)$$

where  $R_{\text{stator}}$  is the radius of the pole tip.

In the structural meshing (see Fig. 3a), the element size is related to the highest frequency of the noise in the simulation. The required element size of the SRM structure can be expressed as [18]

$$\varepsilon = \frac{1}{n} \times \lambda_B \quad (7)$$

where  $\lambda_B$  is the wavelength of the bending wave and  $n$  is the number of elements per wavelength. The number of elements per wavelength is determined by the type of elements in the SRM meshed structure. For linear elements,  $n$  can be between 8 and 10. For quadratic elements,  $n$  is between 4 and 6. Fig. 12 shows the linear elements and quadratic elements. For linear tetrahedron element, shown in Fig. 12a, it needs four interpolation nodes and the shape function is a first-order function. For quadratic tetrahedron element (see Fig. 12b), it needs ten nodes with a second-order shape function.

The wavelength  $\lambda_B$  can be calculated as

$$\lambda_B = \frac{c_B}{f} \quad (8)$$

where  $c_B$  is the speed of the bending sound wave,  $f$  is the maximum frequency in the acoustic simulation. The speed of bending wave,  $c_B$ , can be calculated by

$$c_B = (1.8 \times c_L \times t \times f)^{0.5} \quad (9)$$

where  $c_L$  is the longitudinal sound wave,  $t$  is the thickness of the housing. The speed of the longitudinal wave,  $c_L$ , is calculated as

$$c_L = \left\{ \frac{E}{\rho\pi(1-\nu^2)} \right\}^{0.5} \quad (10)$$

where  $E$ ,  $\rho$  and  $\nu$  are the Young's modulus, density and Poisson's ratio of the housing material, respectively.

The acoustic meshing in ACTRAN includes the meshing of the far field, near field and the coupling surfaces. The element size in the acoustic meshing also depends on the highest frequency of the acoustic noise in the simulation. The element size decreases dramatically when the frequency increases. The maximum frequency simulated in this paper is 10 kHz. The element size in the acoustic meshing can be calculated by

$$\varepsilon = \frac{c}{n \times f} \quad (11)$$

where  $c$  is the speed of the sound,  $f$  is the highest frequency of the acoustic noise,  $n$  is the number of elements per wavelength. For linear elements,  $n$  should be equal to 8–10. For quadratic elements,  $n$  should be equal to 4–6. Given that enough elements per wavelength are used, the linear element mesh and quadratic element mesh should give the same results. The quadratic mesh is usually preferred because it can give more accurate results for a complex geometry or complex acoustic field.

### 3.5 Considerations for the contacts in the meshed structure

Another important issue in the meshing of the structure is the connection of the nodes in the interface between parts. The connections of the nodes at the interfaces affect the stiffness of the parts and affect the natural frequency. Therefore, it is important to model the connections correctly as it will affect the structural behaviour and, hence, affect the acoustics. The connection of the nodes can be defined by the type of contacts between parts. In the 24/16 SRM, the assembly includes the stator core and the housings. Since the inner housing and the outer housing are welded together, the contact between them should be defined as a bonded contact. The subassembly of the stator and the windings can be seen in Fig. 13a. Although there is a thin layer of insulation paper between the coils and the stator poles, the contact between the coils and the stator poles is treated as a bonded contact. This is because vacuum pressure impregnation has been applied to the stator windings. On the other hand, the windings have more mass effect on the stator poles than stiffness effect [13]. The weak stiffness can be simulated by assigning a low value of Young's modulus to the windings, which are in bonded contact with the stator poles. In this paper, the Young's modulus of the winding is 12 GPa [13], which is much lower than the Young's modulus of copper, 117 GPa. More material properties are shown in Table 2.

The connection between the stator core and the housing is treated as a bonded contact because the press fit is used between

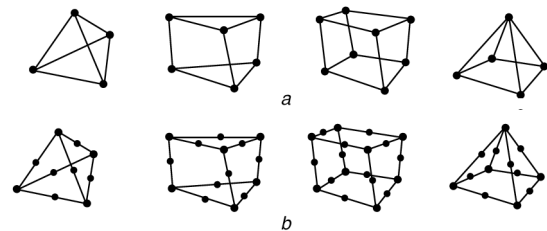
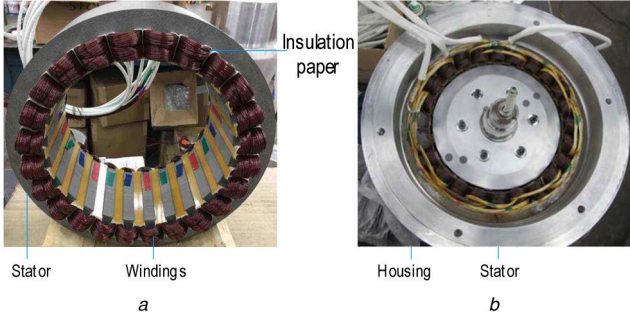


Fig. 12 Element types of the meshing (a) Linear elements, (b) Quadratic elements



**Fig. 13** Contacts between parts  
(a) Bonded contacts in stator-windings subassembly, (b) Bonded contacts between stator and housing

**Table 2** Material properties of the 24/16 SRM

Part	Stator	Coils	Housing
density (kg/m <sup>3</sup> )	7268	4908	2700
Young's modulus (GPa)	176	12	68.9
Poisson's ratio	0.285	0.3	0.33

the housing and the stator core. Another reason is that two small set screws are installed in the interface between the stator core and the housing to avoid tiny relative motion between these two parts.

## 4 Acoustic noise analysis of the 24/16 traction SRM

### 4.1 Dominant harmonics and vibration mode at 2000 rpm

The harmonics of the radial force on the stator core mainly cause the vibration and the acoustic noise in SRMs [19–21]. Analysing the dominant harmonics of the radial force is important for the acoustic noise analysis and noise reduction. It helps to develop a deep understanding of the dominant harmonics and the dominant vibration modes in the 24/16 SRM at a certain speed. In this section, the nodal force at the stator pole tips (see Fig. 7) is extracted to perform the 2D FFT. The 2D nodal force changes with time and stator spatial (or circumferential) position. The radial force is the sum of the harmonics and it can be expressed as [7]

$$\begin{aligned} \mathcal{F}_r(t, \alpha) &= \sum_{v=-\infty}^{\infty} \sum_{u=-\infty}^{\infty} (\mathcal{F}_{r(u,v)}) \\ &= \sum_{v=-\infty}^{\infty} \sum_{u=-\infty}^{\infty} [F_{r(u,v)} \cos(2\pi f_{\text{mech}} u t + v\alpha + \phi_{(u,v)})] \end{aligned} \quad (12)$$

where  $F_r(a, t)$  is the radial force changing with time and stator spatial position,  $F_{r(u,v)}$  is the amplitude of the harmonics,  $f_{\text{mech}}$  is the mechanical frequency,  $u$  is the temporal order,  $v$  is the spatial order,  $t$  is the time,  $\alpha$  is the stator circumferential angle,  $\phi_{(u,v)}$  is the phase angle of the harmonic. The forcing frequency  $f_{f(u,v)}$  of the harmonics can be calculated by  $f_{f(u,v)} = u \times f_{\text{mech}}$ . The mechanical frequency  $f_{\text{mech}}$  is calculated by  $f_{\text{mech}} = n/60$ , where  $n$  is the operating speed of the motor.

The amplitudes of the harmonics are shown in Fig. 14. The harmonics with the same absolute value of  $u$  and the same absolute value of  $v$  can be superimposed based on their phase angles. The superimposed harmonics are summarised in Fig. 15, where  $q$  is the absolute value of  $u$ , and circ equals to the absolute value of  $v$ . In Fig. 15, the harmonics with '+' sign means that the harmonics are rotating in the positive (counter clockwise) direction while the harmonics with '-' sign means that the harmonics are rotating in negative (clockwise) direction. Standing wave is generated in some harmonics. Standing wave is defined as the wave in which the amplitudes of some particular points remain unchanged while other points oscillate.

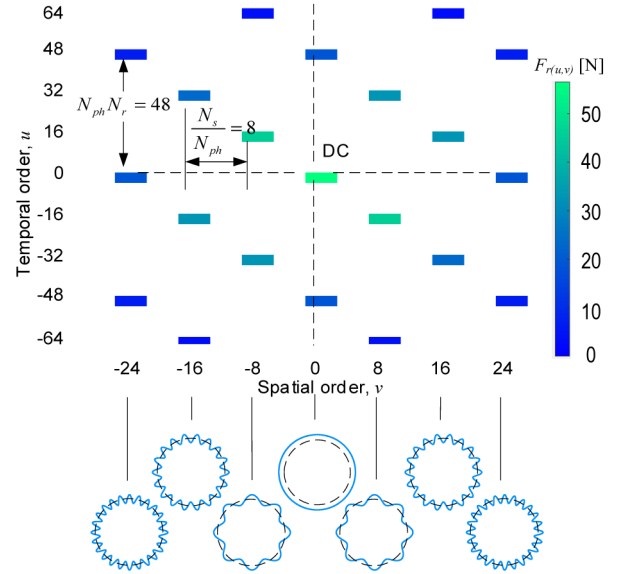


**Fig. 14** Harmonics of the radial nodal force on the stator pole tip, 2000 rpm

$F_{r(\text{circ}, q)}$		Spatial order, $ v  = \text{circ}$			
Forcing frequency	Temporal order, $ u  = q$	0	8	16	24
4800	144	$2F_{r(144, 0)}$			$-2F_{r(48, 24)} + 2F_{r(-48, 24)}$ Standing wave
4267	128		$-2F_{r(128, 8)} + 2F_{r(-128, 16)}$		
3733	112		$+2F_{r(-112, 8)} - 2F_{r(112, 16)}$		
3200	96	$2F_{r(96, 0)}$			$-2F_{r(48, 24)} + 2F_{r(-48, 24)}$ Standing wave
2667	80		$-2F_{r(80, 8)} + 2F_{r(-80, 16)}$		
2133	64		$+2F_{r(-64, 8)} - 2F_{r(64, 16)}$		
1600	48	$2F_{r(48, 0)}$			$-2F_{r(48, 24)} + 2F_{r(-48, 24)}$ Standing wave
1067	32		$-2F_{r(32, 8)} + 2F_{r(-32, 16)}$		
533	16		$+2F_{r(-16, 8)} - 2F_{r(16, 16)}$		
0	0	$F_{r(0, 0)}$			$2F_{r(24, 0)}$

**Fig. 15** Amplitudes of the harmonics in a 24/16 SRM, 2000 rpm

The spatial order,  $v$  is related to the shape of the harmonics [22, 23]. For example, the harmonic  $F_{r(q=48, \text{circ}=0)}$  has a spatial order of 0. When this harmonic is applied to the stator, the shape of the harmonic is concentric to the centre of the stator. The harmonic  $F_{r(q=32, \text{circ}=8)}$  has a spatial order of 8. When this harmonic is applied to the stator, the shape of the harmonic has eight peaks and eight troughs in the circumferential position.

Therefore, the shape of the harmonics with the spatial order  $v=0$  is the same as the vibration mode circ=0. Provided that the forcing frequency,  $u$  of the harmonic is non-zero, this harmonic with  $v=0$  can excite the vibration mode circ=0. Similarly, the shape of the harmonics with a spatial order of 8, 16 and 24 is the same as the vibration mode circ=8, 16 and 24, respectively. Provided that the forcing frequency of these harmonics is non-zero, they can excite the vibration modes circ=8, 16 and 24, respectively. After the superposition of the harmonics, the amplitudes of the dominant harmonics in the 24/16 SRM are shown in Fig. 16. In the 24/16 SRM, the amplitude of the harmonic  $F_{r(q=16, \text{circ}=16)}$  is the largest at 2000 rpm among all the harmonics. However, the harmonic with the highest magnitude might change at different speeds and in different designs with the same pole configuration. For the harmonics with the same circumferential order, the amplitude tends to reduce when the temporal order increases.

### 4.2 Natural frequencies and mode shapes

The natural frequencies,  $\omega_n$ , and the corresponding vibration mode shapes can be calculated and simulated by the numerical method in ACTRAN. In the numerical simulation, the boundary condition is clamped-free, in which the displacement of one end surface of the

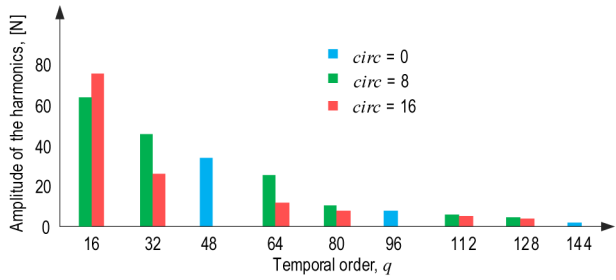


Fig. 16 Comparison of the amplitudes of major harmonics

Table 3 Natural frequencies in different circumferential modes calculated by the method of modal extraction in ACTRAN, unit (Hz)

Vibration mode (circ, ax)	(0,1)	(2,1)	(3,1)	(4,1)	(5,1)	(8,1)
natural frequency	4784	1782	4123	6810	9637	14,963

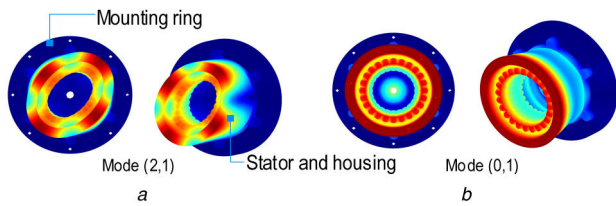


Fig. 17 Vibration mode shapes (a) Mode (2,1), (b) Mode (0,1)

housing is constrained while the other end of the motor is free to vibrate. The mode shapes can be distinguished by the deformation in the circumferential and axial direction. Therefore, the corresponding natural frequencies are with different axial and circumferential orders. Table 3 shows the natural frequencies with the same axial order, 1, but with different circumferential orders. The mode shapes of vibration modes (2,1) and (0,1) are shown in Fig. 17. Vibration mode (0,1), whose natural frequency is 4784 Hz, has a circumferential order of 0, and an axial order of 1.

### 4.3 Surface displacement and acoustic noise

As discussed in the previous section, the harmonics with a spatial order of 0, 8, 16 are the major harmonics that lead to vibration and acoustic noise in the 24/26 SRM at 2000 rpm. The damping ratio used in the simulation of vibration and acoustic noise is calculated by [5]

$$\zeta_{\text{circ}} = \frac{1}{2\pi}(2.76 \times 10^{-5} f_{\text{circ}} + 0.062) \quad (13)$$

where  $\zeta_{\text{circ}}$  is the modal damping ratio,  $f_{\text{circ}}$  is the natural frequency of the mode circ.

An averaged damping ratio is used in this paper by averaging the modal damping ratio of the vibration mode circ = 0 and circ = 8. The modal damping ratio of the vibration mode circ = 16 is not included in the calculation of the averaged damping ratio because the natural frequency of mode circ = 16 exceeds 20 kHz, which would lead to an overestimated damping ratio.

The displacement measured by a virtual displacement sensor, which is mounted on the housing surface, is shown in Fig. 18a. The location of this virtual displacement sensor is shown in Fig. 4b. In the coupled simulation of vibration and noise, the 24/16 SRM starts its operation at  $t=0$  ms and stops at  $t=7.5$  ms. Fig. 18b shows the sound pressure captured by a virtual microphone (see Fig. 4a). The sound pressure starts to be captured at  $t=2.14$  ms, because the distance between the virtual microphone and the housing outer surface is 0.726 m and it takes 2.14 ms for the transmission of the sound wave from the housing surface to the virtual microphone. The value of 2.14 ms can also be calculated by the distance of 0.726 m divided by the speed of air, 340 m/s. After the motor stops at the time step  $t=7.5$  ms, sound wave can still be captured from

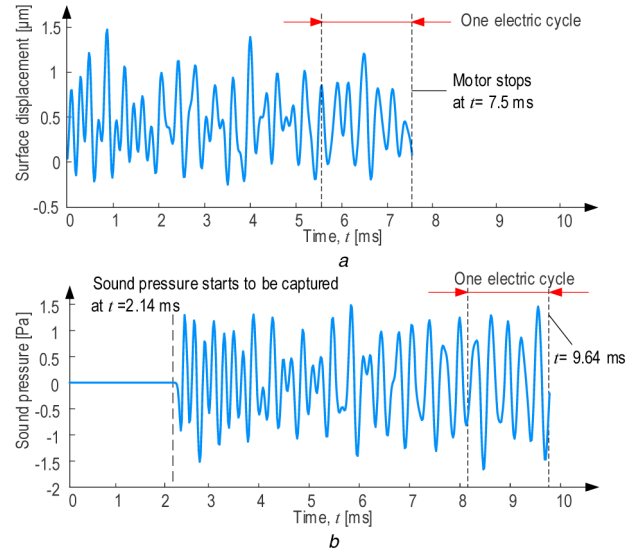


Fig. 18 Vibration and acoustic noise of the 24/16 SRM at 2000 rpm (a) Displacement measured by a sensor on the housing outer surface, (b) Sound pressure measured by a microphone located 1 m away from the motor centre

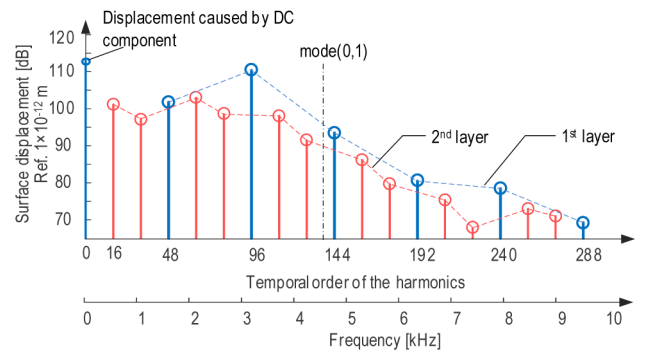


Fig. 19 Surface displacement of the 24/16 SRM at 2000 rpm

the time step  $t=7.5$  ms to the time step  $t=9.64$  ms. This is because the sound wave, which is caused by the vibration of the housing surface at the time step  $t=7.5$  ms, needs 2.14 ms to transmit from the housing outer surface to the virtual microphones.

The surface displacement in Fig. 18a is used for the FFT analysis. The minimum required temporal length of the surface displacement for the FFT analysis is one electric cycle rather than a complete mechanical cycle. Therefore, in order to reduce the computation cost, the coupled simulation of surface displacement and acoustic noise can be shortened to one electrical cycle.

The surface displacement in the frequency domain is shown in Fig. 19. There are two layers. The first layer is the displacements caused by the harmonics  $F_{r(q=48, \text{circ}=0)}$ ,  $F_{r(q=96, \text{circ}=0)}$ ,  $F_{r(q=144, \text{circ}=0)}$ ,  $F_{r(q=192, \text{circ}=0)}$ ,  $F_{r(q=240, \text{circ}=0)}$  and  $F_{r(q=288, \text{circ}=0)}$ . These harmonics have the same circumferential order. They only excite the vibration mode circ = 0, which has a circumferential order zero.

Although the forcing frequency of  $F_{r(q=144, \text{circ}=0)}$  is closer to the natural frequency of the vibration mode circ = 0, the amplitude of the harmonic  $F_{r(q=96, \text{circ}=0)}$  is much higher than that of  $F_{r(q=144, \text{circ}=0)}$  (see Fig. 16). For this reason, This layer peaks at 3200 Hz, which is caused by the harmonic  $F_{r(q=96, \text{circ}=0)}$ . The amplitudes of the harmonics  $F_{r(q=48, \text{circ}=0)}$ ,  $F_{r(q=96, \text{circ}=0)}$ ,  $F_{r(q=144, \text{circ}=0)}$  decrease as they have higher temporal order (see Fig. 16). Therefore, the amplitude of the displacement decreases after 3200 Hz.

The displacement of the second layer is caused by the harmonics with the spatial order 8 and the harmonics with the spatial order 16, simultaneously. For example, the displacement at 533.33 Hz is caused by the harmonics  $F_{r(q=16, \text{circ}=8)}$  and

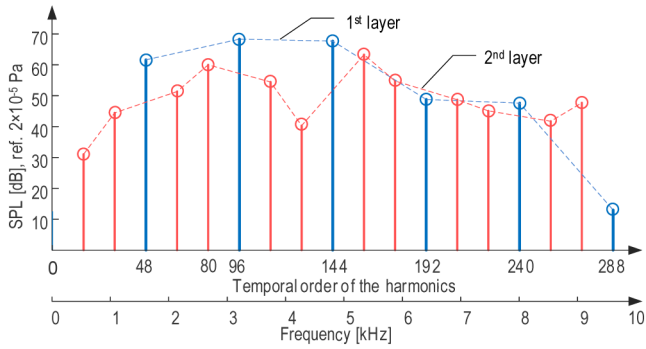


Fig. 20 SPL of the 24/16 SRM at 2000 rpm



Fig. 21 Setup for the hammer test of the 24/16 SRM  
(a) 24/16 SRM mounted in the dyno, (b) Audio interface and power supply

$F_{r(q=16, circ=16)}$  with the same temporal order, 16. This can be verified by the FFT of the nodal force shown in Fig. 15.

By averaging the sound pressure measured by the 20 microphones on a hemisphere, the averaged sound pressure is obtained. The locations of the virtual microphones were shown in Figs. 4 and 5. Then the averaged sound pressure is used for the FFT decomposition. The sound pressure level (SPL) of the 24/16 SRM at 2000 rpm is shown in Fig. 20. Since the acoustic noise is caused by the surface displacement, there are also two layers in the SPL as well. Similar to the surface displacement, the first layer is caused by the harmonics  $F_{r(q=48, circ=0)}$ ,  $F_{r(q=96, circ=0)}$ ,  $F_{r(q=144, circ=0)}$ ,  $F_{r(q=192, circ=0)}$ ,  $F_{r(q=240, circ=0)}$  and  $F_{r(q=288, circ=0)}$ .

The SPL of the 24/16 SRM has two maximum values at the frequencies of 3200 and 4800 Hz, which are caused by the harmonics of  $F_{r(q=96, circ=0)}$  and  $F_{r(q=144, circ=0)}$ . This is because the motor is spinning at a low speed, 2000 rpm, which leads to low forcing frequencies in  $F_{r(q=96, circ=0)}$  and  $F_{r(q=144, circ=0)}$ . In this case, a large magnitude of acoustic noise is generated when the forcing frequencies of  $F_{r(q=96, circ=0)}$  (3200 Hz, see Fig. 15) and  $F_{r(q=144, circ=0)}$  (4800 Hz, see Fig. 15) are close to the natural frequency of the vibration mode  $circ=0$ . Although the surface displacement caused by  $F_{r(q=144, circ=0)}$  is much smaller than that caused by  $F_{r(q=96, circ=0)}$  (see Fig. 19), the SPL caused by  $F_{r(q=144, circ=0)}$  is close to that of  $F_{r(q=96, circ=0)}$  because  $F_{r(q=144, circ=0)}$  has a higher forcing frequency.

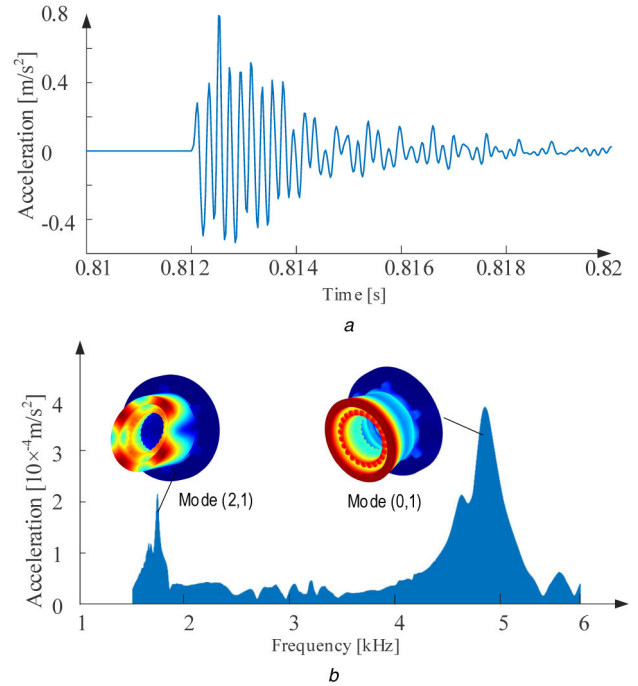


Fig. 22 Hammer test of the 24/16 SRM  
(a) Response in the time domain, (b) Response in the frequency domain

There are two peaks in the second layer of the SPL in Fig. 20, which appear at 2666 and 5333 Hz. The acoustic noise generated in this layer is due to the harmonics exciting the vibration modes  $circ=8$  and  $circ=16$ . The SPL at this layer is caused by harmonics with the spatial order 8 and 16, simultaneously.

## 5 Experimental results

In order to validate the numerical model of the 24/16 SRM, the natural frequency of the experimental motor has been analysed. For the 24/16 SRM, vibration mode (0,1) is the dominant vibrating mode. Its excitation, which is caused by the dominant harmonics of the radial force density, contributes mainly to the acoustic noise of the 24/16 SRM in this paper. Therefore, the natural frequency of vibration mode (0,1) has been validated experimentally through a hammer test.

The setup for the hammer test of the 24/16 SRM is shown in Fig. 21. An accelerometer is mounted on the surface of the motor to measure the response of the surface acceleration.

The response of the accelerometer in the time domain is shown in Fig. 22a. After the FFT, the response in the frequency domain can be seen in Fig. 22b. It can be observed that there are two major peaks appearing in 1735 and 4852 Hz. As shown in Table 3, the simulated natural frequencies of vibration modes (2,1) and (0,1) were 1782 and 4784 Hz, respectively. Therefore, there is a good match between the simulated natural frequency and the hammer test result for vibration mode (0,1), which is the dominant vibration mode for the 24/16 SRM in this paper.

## 6 Conclusions

In this paper, a numerical modelling procedure has been presented to predict the vibration and acoustic noise caused by the electromagnetic force in SRMs. This numerical model couples the electromagnetic analysis in JMAG, modal, vibration and acoustic analysis in ACTRAN. Detailed considerations in the modelling to ensure the accuracy of the results and to reduce the computational cost are also presented. This paper also proposes a useful method to quantitatively obtain and analyse the relationships between dominant harmonics of the radial electromagnetic force, dominant vibration mode, vibration (or surface displacement) and the radiated acoustic noise of an SRM. The acoustic results for a 24/16 SRM at 2000 rpm are shown as an example. The harmonics with a spatial order  $circ=0$  is found to excite the vibration mode  $circ=0$

and cause the maximum vibration and acoustic noise for a 24/16 SRM at 2000 rpm. Harmonics with high temporal order in the 24/16 SRM can lead to noise and vibration when the motor is operating at a low and medium speed.

The modelling and analysis methods in this paper help the designers to effectively evaluate the acoustic behaviour in SRMs, which is the basis of optimizing the structure and the control algorithm to reduce noise and vibration. The numerical modelling presented in this paper can also be applied to other SRM topologies or electric machines.

## 7 Acknowledgments

This research was undertaken, in part, thanks to funding from the Canada Excellence Research Chairs (CERC) Program, Natural Sciences and Engineering Research Council of Canada (NSERC). The authors gratefully acknowledge Free Field Technologies (FFT), Powersys Solutions, CMC Microsystems and ANSYS for their support with ACTRAN software, JMAG software, Solidworks and ANSYS Workbench in this research, respectively.

## 8 References

- [1] Jiang, J.W., Bilgin, B., Emadi, A.: 'Three-phase 24/16 switched reluctance machine for a hybrid electric powertrain', *IEEE Trans. Transport. Electrific.*, 2017, **3**, (1), pp. 76–85
- [2] Bilgin, B., Emadi, A.: 'Electric motors in electrified transportation: a step toward achieving a sustainable and highly efficient transportation system', *IEEE Power Electron. Mag.*, 2014, **1**, (2), pp. 10–17
- [3] Emadi, A.: *Energy-efficient electric motors: selection and applications* (Marcel Dekker, New York, NY, USA, 2004)
- [4] Cai, W., Pillay, P.: 'Resonant frequencies and mode shapes of switched reluctance motors', *IEEE Trans. Energy Convers.*, 2001, **16**, (1), pp. 43–48
- [5] Gieras, J.F., Wang, C., Lai, J.C.: *Noise of polyphase electric motors* (CRC press, Boca Raton, FL, USA, 2005)
- [6] Finley, W.R., Hodowanec, M.M., Holter, W.G.: 'An analytical approach to solving motor vibration problems', *IEEE Trans. Ind. Appl.*, 2000, **36**, (5), pp. 217–232
- [7] Dong, J., Jiang, J., Howey, B., *et al.*: 'Hybrid acoustic noise analysis approach of conventional and mutually coupled switched reluctance motors', *IEEE Trans. Energy Convers.*, 2017, **32**, (3), pp. 1042–1051
- [8] Zhu, Z.Q., Liu, X., Pan, Z.: 'Analytical model for predicting maximum reduction levels of vibration and noise in switched reluctance machine by active vibration cancellation', *IEEE Trans. Energy Convers.*, 2011, **26**, (1), pp. 36–45
- [9] Anwar, M.N., Husain, I.: 'Radial force calculation and acoustic noise prediction in switched reluctance machines', *IEEE Trans. Ind. Appl.*, 2000, **36**, (6), pp. 1589–1597
- [10] Putri, A.K., Rick, S., Franck, D., *et al.*: 'Application of sinusoidal field pole in a permanent-magnet synchronous machine to improve the NVH behavior considering the MTPA and MTPV operation area', *IEEE Trans. Ind. Appl.*, 2016, **52**, (3), pp. 2280–2288
- [11] Takiguchi, M., Sugimoto, H., Kurihara, N., *et al.*: 'Acoustic noise and vibration reduction of SRM by elimination of third harmonic component in sum of radial forces', *IEEE Trans. Energy Convers.*, 2015, **30**, (3), pp. 883–891
- [12] dos Santos, F. L. M., Anthonis, J., Naclerio, F., *et al.*: 'Multiphysics NVH modeling: simulation of a switched reluctance motor for an electric vehicle', *IEEE Trans. Ind. Electron.*, 2014, **61**, (1), pp. 469–476
- [13] Bösing, M.: 'Acoustic modelling of electrical drives'. PhD thesis, RWTH Aachen Univ., December 2013
- [14] Lin, C., Fahimi, B.: 'Prediction of acoustic noise in switched reluctance motor drives', *IEEE Trans. Energy Convers.*, 2014, **29**, (1), pp. 250–258
- [15] Castano, S.M., Bilgin, B., Fairall, E., *et al.*: 'Acoustic noise analysis of a high-speed high-power switched reluctance machine: frame effects', *IEEE Trans. Energy Convers.*, 2016, **31**, (1), pp. 69–77
- [16] Marburg, S., Nolte, B.: *Computational acoustics of noise propagation in fluids: finite and boundary element methods* (Springer, Berlin, Germany, 2008)
- [17] Astley, R.J., Coyette, J.P.: 'The performance of spheroidal infinite elements', *Int. J. Numer. Methods Eng.*, 2001, **52**, (12), pp. 1379–1396
- [18] Norton, M.P., Karczub, D.G.: *Fundamentals of noise and vibration analysis for engineers* (Cambridge University Press, Cambridge, UK, 2003)
- [19] Guo, X., Zhong, R., Zhao, L., *et al.*: 'Method for radial vibration modelling in switched reluctance motor', *IET Electr. Power Appl.*, 2018, **8**, (1), pp. 12–19
- [20] Castano, M.S., Bilgin, B., Lin, J., *et al.*: 'Radial forces and vibration analysis in an external-rotor switched reluctance machine', *IET Electr. Power Appl.*, 2016, **11**, (2), pp. 252–259
- [21] Guo, X., Zhong, R., Ding, D., *et al.*: 'Origin of resonance noise and analysis of randomising turn-on angle method in switched reluctance motor', *IET Electr. Power Appl.*, 2017, **11**, (7), pp. 1324–1332
- [22] Le Besnerais, J., Lanfranchi, V., Hecquet, M., *et al.*: 'Characterisation of radial vibration force and vibration behaviour of a pulse-width modulation-fed fractional-slot induction machine', *IET Electr. Power Appl.*, 2009, **3**, (3), pp. 197–208
- [23] Le Besnerais, J., Lanfranchi, V., Hecquet, M., *et al.*: 'Multiobjective optimization of induction machines including mixed variables and noise minimization', *IEEE Trans. Magn.*, 2008, **44**, (6), pp. 1102–1105